

# Vapor Phase Synthesis of Organometal Halide Perovskite Nanowires for Tunable Room-Temperature Nanolasers

Jun Xing,<sup>†</sup> Xin Feng Liu,<sup>†,‡</sup> Qing Zhang,<sup>†</sup> Son Tung Ha,<sup>†</sup> Yan Wen Yuan,<sup>†</sup> Chao Shen,<sup>†</sup> Tze Chien Sum,<sup>†,‡,§</sup> and Qihua Xiong<sup>\*,†,§,||</sup>

<sup>†</sup>Division of Physics and Applied Physics, School of Physical and Mathematical Sciences, Nanyang Technological University, Singapore 637371

<sup>‡</sup>Energy Research Institute @ NTU (ERI@N), Nanyang Technological University, 50 Nanyang Drive, Singapore 637553

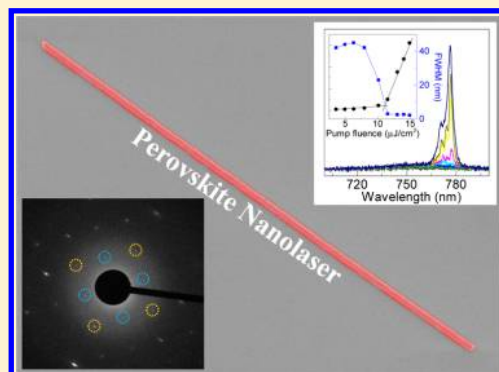
<sup>§</sup>Singapore-Berkeley Research Initiative for Sustainable Energy, 1 Create Way, Singapore 138602

<sup>||</sup>NOVITAS, Nanoelectronics Centre of Excellence, School of Electrical and Electronic Engineering, Nanyang Technological University, Singapore 639798

## S Supporting Information

**ABSTRACT:** Semiconductor nanowires have received considerable attention in the past decade driven by both unprecedented physics derived from the quantum size effect and strong isotropy and advanced applications as potential building blocks for nanoscale electronics and optoelectronic devices. Recently, organic–inorganic hybrid perovskites have been shown to exhibit high optical absorption coefficient, optimal direct band gap, and long electron/hole diffusion lengths, leading to high-performance photovoltaic devices. Herein, we present the vapor phase synthesis free-standing  $\text{CH}_3\text{NH}_3\text{PbI}_3$ ,  $\text{CH}_3\text{NH}_3\text{PbBr}_3$ , and  $\text{CH}_3\text{NH}_3\text{PbI}_x\text{Cl}_{3-x}$  perovskite nanowires with high crystallinity. These rectangular cross-sectional perovskite nanowires have good optical properties and long electron hole diffusion length, which ensure adequate gain and efficient optical feedback. Indeed, we have demonstrated optical-pumped room-temperature  $\text{CH}_3\text{NH}_3\text{PbI}_3$  nanowire lasers with near-infrared wavelength of 777 nm, low threshold of  $11 \mu\text{J}/\text{cm}^2$ , and a quality factor as high as 405. Our research advocates the promise of optoelectronic devices based on organic–inorganic perovskite nanowires.

**KEYWORDS:** Organic–inorganic perovskites, nanowire, photoluminescence spectroscopy, nanolasers



Organic–inorganic hybrid perovskites, the structural analogues of calcium titanium oxide crystal, have been widely studied due to their unique structure of alternating stacking sheet of organic and inorganic components.<sup>1–3</sup> Recently, considerable progress has shown that those perovskites exhibit high optical absorption coefficient, optimal direct band gap and long electron/hole diffusion lengths ranging from 100 nm to 175  $\mu\text{m}$ , which underpin the increasingly high performance in solar cells.<sup>4–7</sup> Specifically, the lead halide perovskite  $\text{CH}_3\text{NH}_3\text{PbX}_3$  ( $\text{X} = \text{Cl}, \text{Br}, \text{and I}$ ) thin film solar cells have reached a record-high efficiency of 20.1% in the past five years.<sup>8–13</sup> Furthermore, the good optical and electrical transport properties of the organic–inorganic perovskites make them also suitable for other optical, electronic, and optoelectronic devices, such as light-emitting diodes, lasers, photodetectors, and field-effect transistors.<sup>14–22</sup> In general, these applications are largely determined by the crystalline quality and the structure of the materials. Perovskites with reduced dimensionality, for instance, two-dimensional crystals, have shown excellent optical properties leading to sufficient gain toward whispering gallery mode lasing.<sup>15</sup> One-dimensional nanowires synthesized by wet chemistry have also attracted

some attention in solar cells and photodetectors.<sup>20,23</sup> Compared to polycrystalline thin film, low-dimensional layered crystals or nanowires exhibit higher crystalline quality thus longer carrier diffusion length, larger gain for lower threshold applications. Therefore, they are expected to play an important role as potential building blocks for the nanoscale optical, electronic, and optoelectronic devices in future based on the emergent perovskite materials.

Herein, we report the synthesis of high crystalline quality  $\text{CH}_3\text{NH}_3\text{PbI}_3$  nanowires with rectangular block morphology and length up to 20  $\mu\text{m}$  by a two-step vapor phase method, using  $\text{PbI}_2$  and  $\text{CH}_3\text{NH}_3\text{I}$  as precursors. Temperature-dependent photoluminescence (PL) spectroscopy on individual nanowires is conducted to investigate the optical properties. The high quality  $\text{CH}_3\text{NH}_3\text{PbI}_3$  nanowire constitutes a built-in Fabry–Pérot microresonator and we have demonstrated the strong optical-pumped room-temperature lasing with near-infrared wavelength of 777 nm, low threshold of  $11 \mu\text{J}/\text{cm}^2$ ,

**Received:** March 25, 2015

**Revised:** May 22, 2015

**Published:** June 4, 2015

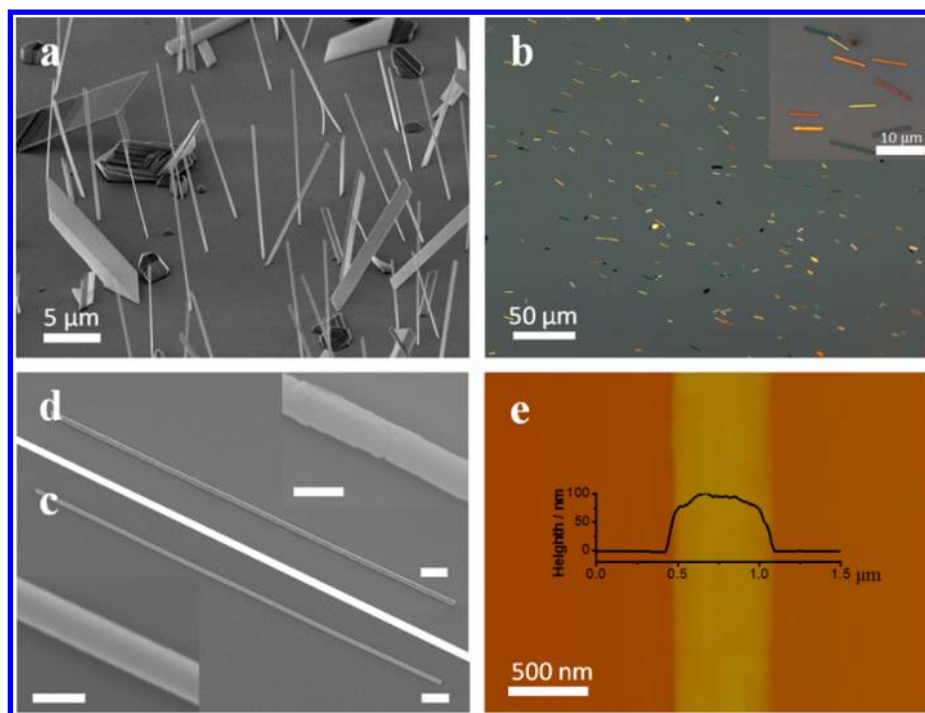


**Figure 1.** (a) SEM image of  $\text{PbI}_2$  nanowires grown on silicon substrate. (b) Optical microscopy image of  $\text{CH}_3\text{NH}_3\text{PbI}_3$  nanowires on silicon substrate. Inset in (b) is the magnified image. SEM images of  $\text{PbI}_2$  nanowire (c) and its corresponding conversion product  $\text{CH}_3\text{NH}_3\text{PbI}_3$  nanowire (d). Insets in (c) and (d) are their corresponding magnified SEM images. Scale bars in (c,d) and their insets are  $2\ \mu\text{m}$  and  $500\ \text{nm}$ , respectively. (e) AFM image of the  $\text{CH}_3\text{NH}_3\text{PbI}_3$  nanowire lies flat on silicon substrate.

and a quality factor as high as 405. Here, the threshold is nearly 4 times lower than that of the  $\text{CH}_3\text{NH}_3\text{PbI}_3$  nanoplates in our previous report.<sup>15</sup> By replacing  $\text{CH}_3\text{NH}_3\text{I}$  with  $\text{CH}_3\text{NH}_3\text{Br}$  or  $\text{CH}_3\text{NH}_3\text{Cl}$ , we can tune the lasing wavelength from 777 to 551 and 744 nm, respectively.

The perovskite nanowires are synthesized by a two-step vapor phase synthesis method. Briefly,  $\text{PbI}_2$  nanowires were first synthesized on silicon oxide substrates by chemical vapor deposition (CVD) method with the central zone temperature of  $380\ ^\circ\text{C}$  and substrates mounted  $\sim 12\ \text{cm}$  downstream of the furnace. Consequently,  $\text{PbI}_2$  was converted into halide perovskite through a gas–solid heterophase reaction with ammonium halide molecules (see Methods).<sup>24</sup> Figure 1a and Supporting Information Figure S1a are the scanning electron microscopy (SEM) images of the as-grown  $\text{PbI}_2$  on silicon substrate, illustrating that  $\text{PbI}_2$  nanowires and bulk crystals are simultaneously grown on the silicon oxide surface. However, the nanowire morphology is dominant. Further analysis (Supporting Information Figure S1b–d) suggests that the  $\text{PbI}_2$  nanowires grew vertically on silicon substrate and exhibit a rectangular or nearly square cross section with the aspect ratio ranging from 1 to 20. To obtain high density and uniform  $\text{PbI}_2$  nanowires laid down on substrates for optical studies, a dry transfer method was used to separate the nanowire from the growth silicon substrate. We put another new silicon substrate on the top of the substrate grown  $\text{PbI}_2$ , then slightly pressed it from top and finally separated two silicon wafers. According to optical microscopy observation (Supporting Information Figure S2a), we confirm that only  $\text{PbI}_2$  nanowires are transferred onto silicon wafer. That is probably because of the intermolecular forces between the substrates and the flat  $\text{PbI}_2$  nanowire surfaces. This dry transfer process can be applied to other planar substrates, such as quartz, indium tin oxide, and polymer substrates, which eliminates the common dispersion in polar

solutions that is not compatible with  $\text{PbI}_2$  and reduces the quality of the subsequent product of  $\text{CH}_3\text{NH}_3\text{PbI}_3$  perovskites.

Transmission electron microscopy (TEM) was used to further characterize the crystalline structure of the as-synthesized  $\text{PbI}_2$  nanowire. As shown in Figure 2a, the nanowire has a uniform contrast, confirming that the rectangular structure of  $\text{PbI}_2$  nanowire. The high-resolution TEM (HRTEM) image (Figure 2b) exhibits clear fringes parallel with spacing of 0.394 and 0.226 nm, which are corresponding to  $(1\bar{2}10)$  and  $(10\bar{1}0)$  lattice spacing of hexagonal  $\text{PbI}_2$  crystal, respectively. On the basis of the observed fringes along the three directions, the white hexagon drawn in Figure 2b shows the six relevant crystal facets being perpendicular to the  $c$ -axis of the  $\text{PbI}_2$  crystal. The lattice fringe can be identified continuously across the entire surface, indicating that the  $\text{PbI}_2$  nanowire has a single-crystalline characteristic. Furthermore, the single crystalline character of the  $\text{PbI}_2$  nanowire can also be predicated from the selected area electron diffraction (SAED) pattern in inset of Figure 2a. According to analysis of the SAED result, it can be concluded that the  $\text{PbI}_2$  nanowire grows predominantly along the  $[010]$  direction and is closed by the  $(0001)$  and  $(000\bar{1})$  planes on the top and bottom sides. This is also consistent with the HRTEM image (Figure 2b) that clearly shows the  $(1\bar{2}10)$  lattice planes perpendicular to the nanowire growth direction. It can be seen that the SAED patterns show slight elongation of the diffraction spots along  $[010]$  direction. That might be caused by the lattice distortion forming during the organic molecular insertion into the lattice of  $\text{PbI}_2$  crystal.

$\text{CH}_3\text{NH}_3\text{PbI}_3$  perovskite nanowires were formed through intercalating the  $\text{CH}_3\text{NH}_3\text{I}$  molecular into the interval sites of  $\text{PbI}_6$  octahedrons layers. After conversion, the geometry of  $\text{CH}_3\text{NH}_3\text{PbI}_3$  perovskite is still maintained as the nanowire as displayed in SEM images (Figure 1c,d). The difference in color

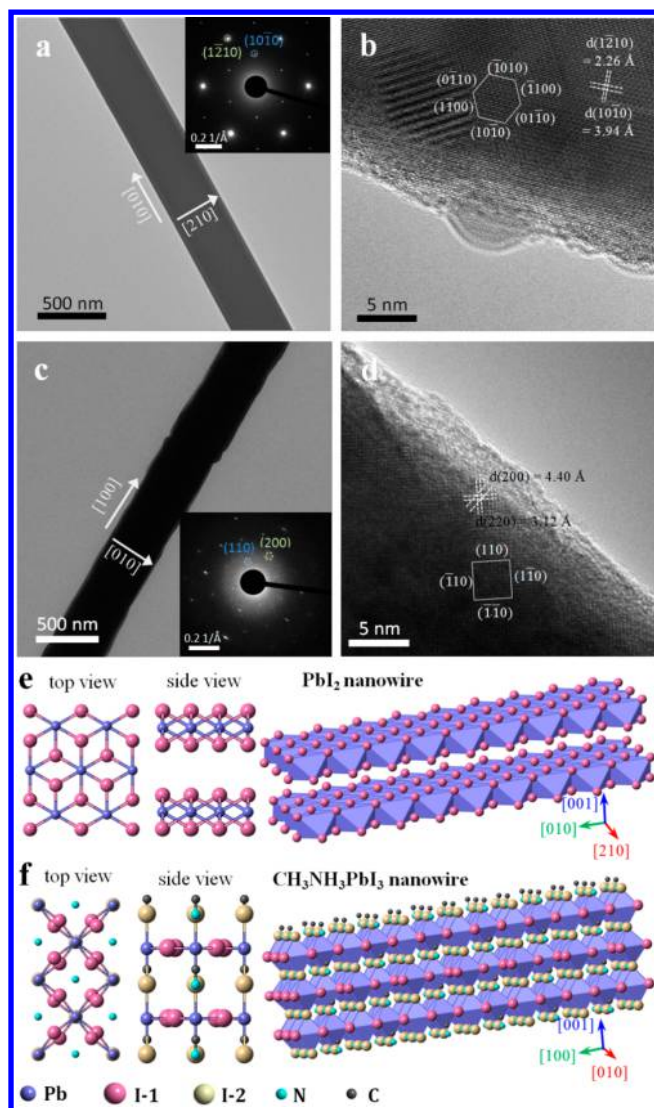


**Figure 2.** TEM and HRTEM images of  $\text{PbI}_2$  nanowire (a,b) and  $\text{CH}_3\text{NH}_3\text{PbI}_3$  nanowire (c,d). Insets in (a,c) are their corresponding SAED patterns. Structure simulation images of  $\text{PbI}_2$  nanowire (e) and  $\text{CH}_3\text{NH}_3\text{PbI}_3$  nanowire (f).

of the perovskite nanowires in the optical microscopy image is attributed to the different interference in the  $\text{CH}_3\text{NH}_3\text{PbI}_3$  nanowire with different thickness (more pronounced in Figure 1b), which has been confirmed by atomic force microscopy (AFM). However, the surface of  $\text{CH}_3\text{NH}_3\text{PbI}_3$  nanowires becomes rough compared to that of the  $\text{PbI}_2$  nanowires. AFM topography also indicates a relatively rough surface of the  $\text{CH}_3\text{NH}_3\text{PbI}_3$  nanowires (Figure 1e). Additional structural characterization of the  $\text{CH}_3\text{NH}_3\text{PbI}_3$  nanowires was carried out using TEM. Figure 2c shows a typical TEM image of a  $\text{CH}_3\text{NH}_3\text{PbI}_3$  nanowire with a width of ca. 500 nm, and its single-crystal character can be determined by the SAED pattern (inset in Figure 2c). According to the SAED analysis, it can be seen that the  $\text{CH}_3\text{NH}_3\text{PbI}_3$  nanowire grows along the  $[100]$  direction and is closed by the  $(001)$  and  $(00\bar{1})$  facet on the top and bottom sides. Furthermore, HRTEM image provides additional evidence for the crystallinity and growth characteristics of  $\text{CH}_3\text{NH}_3\text{PbI}_3$  nanowire. Figure 2d shows the nanowire with clear lattice fringes of 0.312 and 0.440 nm corresponding to the  $(220)$  and  $(200)$  lattice spacing of tetragonal

$\text{CH}_3\text{NH}_3\text{PbI}_3$  crystal. On the basis of the observed fringes, the white square drawn in Figure 2d shows the four relevant crystal facets being perpendicular to the  $c$ -axis of the  $\text{CH}_3\text{NH}_3\text{PbI}_3$  crystal. On the basis of the above analysis, the crystalline structure of the  $\text{PbI}_2$  and  $\text{CH}_3\text{NH}_3\text{PbI}_3$  perovskite nanowires can be simulated in Figure 2e,f.

Furthermore, we also prepared the organic–inorganic perovskite using  $\text{PbI}_2$  nanowire and  $\text{CH}_3\text{NH}_3\text{Br}$  and  $\text{CH}_3\text{NH}_3\text{Cl}$  as precursors by the same method. Energy dispersive X-ray spectroscopy (EDX) was used to probe the elemental composition of these two samples (Supporting Information Figure S3). It can be concluded that Br substituted the I completely when  $\text{CH}_3\text{NH}_3\text{Br}$  molecular reacts with  $\text{PbI}_2$  nanowire, leading to the formation of  $\text{CH}_3\text{NH}_3\text{PbBr}_3$ . Similarly, Cl partially displaced I atoms with  $\text{CH}_3\text{NH}_3\text{Cl}$  molecular insertion into  $\text{PbI}_2$  nanowire to form perovskite  $\text{CH}_3\text{NH}_3\text{PbI}_x\text{Cl}_{3-x}$ . The samples  $\text{CH}_3\text{NH}_3\text{PbBr}_3$  and  $\text{CH}_3\text{NH}_3\text{PbI}_x\text{Cl}_{3-x}$  are also maintained as nanowire morphology (Supporting Information Figure S4). Moreover, we also successfully synthesized  $\text{PbBr}_2$  nanowire on mica substrate (Supporting Information Figure S5), which can be converted into  $\text{CH}_3\text{NH}_3\text{PbI}_x\text{Br}_{3-x}$  and  $\text{CH}_3\text{NH}_3\text{PbBr}_x\text{Cl}_{3-x}$  perovskite nanowires (see Methods).

Figure 3a–c displays the temperature-dependent PL spectra of  $\text{CH}_3\text{NH}_3\text{PbI}_3$ ,  $\text{CH}_3\text{NH}_3\text{PbI}_x\text{Cl}_{3-x}$ , and  $\text{CH}_3\text{NH}_3\text{PbBr}_x\text{Cl}_{3-x}$  respectively. As temperature ( $T$ ) is between 300 and  $\sim 160$  K, only one emission peak was observed with a monotonic peak redshift and width narrowing with the decreasing of the temperature. The photoluminescence of the perovskites can be attributed to the combination of the excited electrons in Pb 6p states and the hole in X ( $X = \text{Cl}, \text{Br}, \text{and I}$ ) out p states.<sup>24</sup> The Pb–X bond distances and connectivity (corner/edge sharing) of infinitely extended  $\text{PbI}_6$  octahedral units influences exciton energies, causing the different emission energy of these perovskites.<sup>6,25</sup> Whether the emission origin of the perovskites is due to free exciton or free carrier is still debated.<sup>14,15</sup> Exciton binding energy was measured or evaluated by various experimental and theoretical pathways, while a broad range of values from several to tens of millielectronvolts were reported. First of all, the low stability of the materials may introduce additional error in widely used optical measurements. Second, because the materials are hybrid organic–inorganic semiconductors, the previous theory or experimental techniques based on traditional inorganic semiconductor may not be sufficient to explain the observations. Because the perovskite family shows high light harvesting and conversion efficiency, a free carrier model at room temperature is more acceptable. As  $T$  is  $\sim 140$ – $150$  K, a new emission peak with a higher energy shows up, which is due to the phase transition of the organolead halide perovskite and the formation of orthorhombic phase as reported previously.<sup>26</sup> When the temperature further decreases from  $\sim 140$ – $77$  K, the higher energy emission peak gains strength in intensity and monotonically shifts to longer wavelengths, whereas the lower energy emission peak gradually becomes relatively weak compared to the higher energy emission peak. It can be seen that as the temperature decreases, both of the two emission peaks redshift. This “Varshni” trend is often observed in lead composite semiconductors.<sup>27</sup> The photoluminescence emission energy  $E_g$  is extracted and plotted in Figure 3f. Interestingly, these three perovskites nanowires have nearly the same value of  $dE_g/dT$  either in high- or low-temperature crystalline phases. Figure 3d shows the temperature-dependent photoluminescence spectra of  $\text{CH}_3\text{NH}_3\text{PbBr}_3$



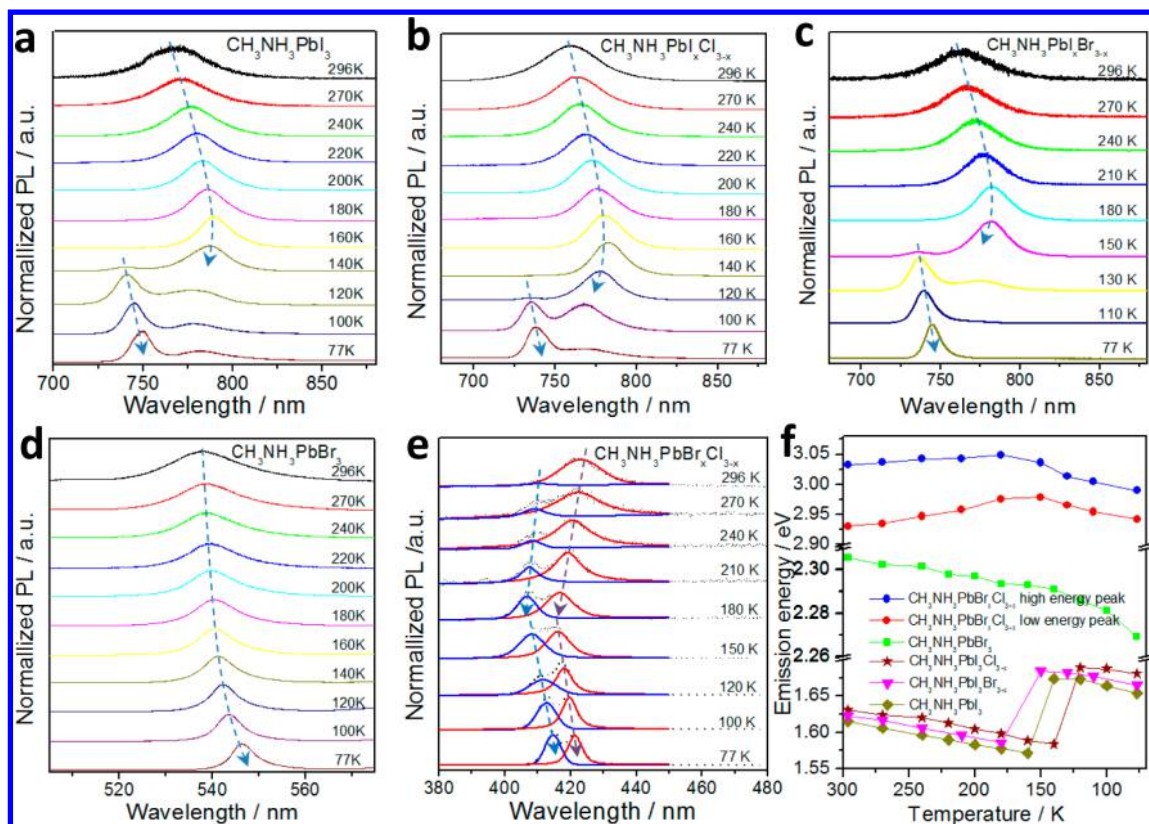


**Figure 3.** (a–e) Temperature-dependent PL spectra taken from 296 to 77 K; for clarity, the intensities of the spectra are normalized. (f) Temperature-dependent emission energy from 296 to 77 K.

nanowires. As  $T$  decreases from 296 to 77 K, only one photoluminescence peak can be resolved with pronounced redshift, indicating the absence of phase transition. Previous X-ray diffraction (XRD) studies show that four phases can be identified for the  $\text{CH}_3\text{NH}_3\text{PbBr}_3$  ( $T > 236.9$  K cubic  $Pm\bar{3}m$ ;  $155.1$  K  $< T < 236.9$  K tetragonal  $I4/m\bar{c}m$  and  $149.5$  K  $< T < 155.1$  K tetragonal  $P4/mmm$ ;  $T < 144.5$  K orthorhombic  $Pna2_1$ ).<sup>28</sup> The mechanism needs to be further investigated. The perovskite  $\text{CH}_3\text{NH}_3\text{PbBr}_x\text{Cl}_{3-x}$  exhibits a very different trend from the above four perovskites. As shown in Figure 3e, the emission from room temperature can be deconvoluted into two individual peaks, possibly due to two kinds of recombination centers. Both of the two peaks blueshift at  $T > 180$  K and then redshift at  $T < 160$  K. This anomalous behavior of peak shift is very similar to some alloys (e.g., InGaN, AlGaIn, and ZnCdO) that show “S”-shaped variation of the photoluminescence peak energy with increasing temperature from 10 K to room temperature.<sup>29,30</sup> In general, these alloy materials have carrier localization effect, which can be ascribed to the potential fluctuation, a consequence of the inhomogeneous composition. At a different temperature region, the photoluminescence shift is dominated by different factors, which causes the different shift trend at a different temperature region. To observe the emission energy of these perovskite nanowires clearly, we summarized the temperature-dependent emission energy in Figure 3f.

Semiconductor nanowires offer the possibility of reducing the size of devices for three-dimensional device integration and therefore are being extensively studied in the context of optoelectronic devices, such as photonic and plasmonic nanolasers and waveguides.<sup>31–38</sup> Perovskites have been suggested to be able to provide sufficient gain toward lasing

and we have recently demonstrated whispering gallery mode lasing at near-infrared wavelength at room temperature.<sup>14,15</sup> In nanowire morphology, a good Fabry–Pérot cavity naturally forms, as such it would be meaningful to explore the Fabry–Pérot lasing in perovskites with facile tuning of wavelength, toward the design of nanoscale optoelectronic devices operating at visible and near-infrared wavelengths. In Figure 4a, we display the PL spectra from a typical  $\text{CH}_3\text{NH}_3\text{PbI}_3$  nanowire (length  $\sim 10$   $\mu\text{m}$  and diameter  $\sim 200$  nm) at a pumping fluence ranging from 3.6 to 15  $\mu\text{J}/\text{cm}^2$ . The integrated output emission and the full width at half-maximum (fwhm) over the whole spectra range as a function of pumping fluence are shown in the inset of Figure 4a, which shows the evolution from a spontaneous emission to lasing behavior. The experiment data (black points) is well fitted by two different linear parts (black line) with a knee at  $P_{\text{ex}} \sim 11$   $\mu\text{J}/\text{cm}^2$ , which is the corresponding lasing threshold  $P_{\text{th}}$ . From the spectra measured at pump fluence above lasing threshold, the mode distance ( $\Delta\lambda$ ) of lasing peak is around 2 nm, which is in good agreement with the theoretical equation  $\Delta\lambda = (1/L)[(\lambda^2/2)(n - \lambda dn/d\lambda)^{-1}]$  for a Fabry–Pérot cavity. The Fabry–Pérot mode of  $\lambda$  (777.0 nm) has a  $\lambda_{\text{fwhm}}$  of  $\sim 1.9$  nm, leading to a corresponding  $Q$ -factor of  $\sim 405$  (Supporting Information Figure S6). Further confirming the lasing action, we note the bright-field image of a single nanowire and the corresponding PL images with an increase in the pump fluence (Figure 4b). When the excitation fluence is below the threshold, the entire nanowire is dim but uniform. However, above the threshold, two bright spots at the distal ends of the nanowire are observed. To investigate the lasing property dependent on temperature, we conducted the lasing actions by decreasing the temperature from 300 to 80 K. It can be seen from Figure 4c that the lasing

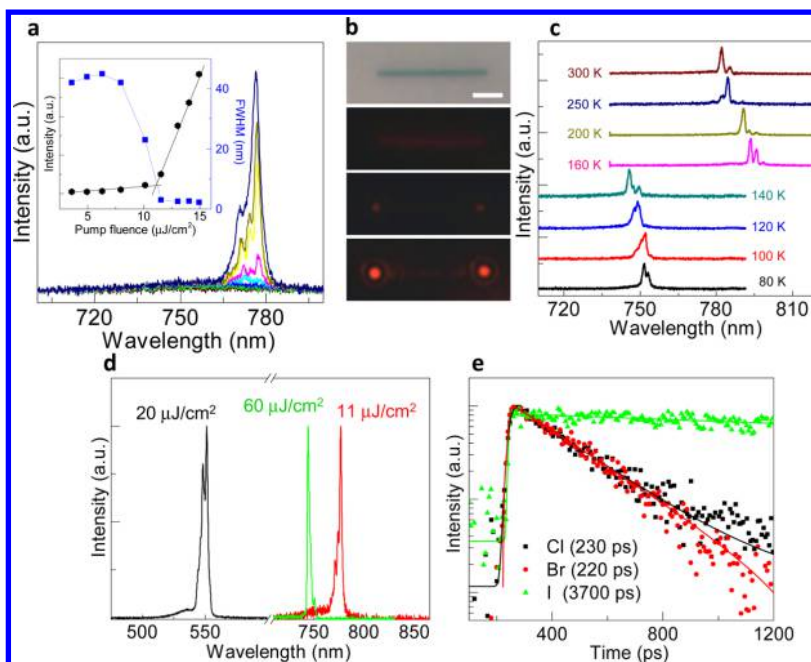


**Figure 4.** (a) The evolution from spontaneous emission to lasing (Fabry–Pérot mode) in a typical  $\text{CH}_3\text{NH}_3\text{PbI}_3$  nanowire. The pumping fluences range from 3.6 to 15  $\mu\text{J}/\text{cm}^2$ . Inset is integrated output emission ( $P_{\text{out}}$ ) and the fwhm over the whole spectra range as a function of pumping fluence ( $P_{\text{ex}}$ ). The experiment data (black points) is well fitted by distinguished functions (black line) with a knee at  $P_{\text{ex}} \sim 11 \mu\text{J}/\text{cm}^2$  (lasing threshold  $P_{\text{th}}$ ).  $\lambda_{\text{fwhm}} \sim 1.9 \text{ nm}$  for Fabry–Pérot mode  $\lambda = 777.0 \text{ nm}$  and the corresponding Q-factor is  $\sim 405$  (Supporting Information Figure S6). (b) The bright-field image of a single  $\text{CH}_3\text{NH}_3\text{PbI}_3$  nanowire and the corresponding PL images with increasing the pump fluences (from below the threshold to above the threshold, false color, the scale bar is 5  $\mu\text{m}$ ). (c) Lasing behavior of single  $\text{CH}_3\text{NH}_3\text{PbI}_3$  nanowire at different temperatures. (d) Lasing spectra of  $\text{CH}_3\text{NH}_3\text{PbI}_3$ ,  $\text{CH}_3\text{NH}_3\text{PbBr}_3$  and  $\text{CH}_3\text{NH}_3\text{PbI}_{1-x}\text{Br}_x$ . For  $\text{CH}_3\text{NH}_3\text{PbBr}_3$ ,  $P_{\text{ex}} = 20 \mu\text{J}/\text{cm}^2$ ,  $\lambda_{\text{fwhm}} \sim 2.0 \text{ nm}$  for Fabry–Pérot mode  $\lambda = 551.3 \text{ nm}$ , and the corresponding Q-factor is  $\sim 225$ . For  $\text{CH}_3\text{NH}_3\text{PbI}_{1-x}\text{Br}_x$ ,  $P_{\text{ex}} = 60 \mu\text{J}/\text{cm}^2$ ,  $\lambda_{\text{fwhm}} \sim 1.6 \text{ nm}$  for Fabry–Pérot mode  $\lambda = 744.4 \text{ nm}$ , and the corresponding Q-factor is  $\sim 372$  (Supporting Information Figure S6). (e) The photoluminescence decay profile of individual  $\text{CH}_3\text{NH}_3\text{PbI}_3$ ,  $\text{CH}_3\text{NH}_3\text{PbBr}_3$ , and  $\text{CH}_3\text{NH}_3\text{PbI}_{1-x}\text{Br}_x$  nanowire.

wavelength always redshifts with the decreasing of temperature; however, the lasing occurs at lower energy side ( $\sim 780 \text{ nm}$ ) above 160 K while occurs at higher energy side below 140 K. This behavior is consistent with the PL measurement results, as shown in Figure 3a, that the lasing peak positions are determined by the gain area. To expand the lasing wavelength, we have also measured the lasing behavior in  $\text{CH}_3\text{NH}_3\text{PbBr}_3$  and  $\text{CH}_3\text{NH}_3\text{PbI}_{1-x}\text{Br}_x$  nanowire samples. The lasing wavelength can be tuned from 777 to 744 nm ( $\text{CH}_3\text{NH}_3\text{PbI}_{1-x}\text{Br}_x$ ) and then 551 nm ( $\text{CH}_3\text{NH}_3\text{PbBr}_3$ ) (Figure 4d). Through precisely tuning the component ratio between Br and Cl (I) in  $\text{CH}_3\text{NH}_3\text{PbBr}_x\text{Cl}_{3-x}$  or  $\text{CH}_3\text{NH}_3\text{PbI}_x\text{Br}_{3-x}$ , fine-tuning of the lasing wavelength can be fulfilled. It should be noted that the lasing threshold for  $\text{CH}_3\text{NH}_3\text{PbBr}_3$  (20  $\mu\text{J}/\text{cm}^2$ ) and  $\text{CH}_3\text{NH}_3\text{PbI}_{1-x}\text{Br}_x$  (60  $\mu\text{J}/\text{cm}^2$ ) is slightly larger than that (11  $\mu\text{J}/\text{cm}^2$ ) in  $\text{CH}_3\text{NH}_3\text{PbI}_3$ , which might be caused by the low losses in the  $\text{CH}_3\text{NH}_3\text{PbI}_3$  for the relatively longer wavelength of emission. Time-resolved photoluminescence measurements are also performed, as shown in Figure 4e; all three curves exhibit single exponential decay. It can be seen that  $\text{CH}_3\text{NH}_3\text{PbI}_3$  has a relatively long lifetime ( $\sim 3.7 \text{ ns}$ ), while shorter lifetimes are observed in  $\text{CH}_3\text{NH}_3\text{PbBr}_3$  ( $\sim 220 \text{ ps}$ ) and  $\text{CH}_3\text{NH}_3\text{PbI}_{1-x}\text{Br}_x$  ( $\sim 230 \text{ ps}$ ) nanowires. When lasing occurs in the nanowire, a very fast lifetime ( $\sim 10 \text{ ps}$ , close to the system time resolution) of  $\text{CH}_3\text{NH}_3\text{PbI}_3$  can be observed as shown in Supporting Information Figure S7. From previous reports, the measured lifetime for  $\text{CH}_3\text{NH}_3\text{PbI}_{1-x}\text{Br}_x$  film is generally in the nanoseconds regime. Through passivation, enhanced lifetime with the magnitude of microseconds is observed in the lead halide perovskite.<sup>39</sup> A high density of defects states always

caused a relatively short lifetime where a large degree of electronic disorder is exhibited. In our nanowire structured samples, due to the special morphology that is not compatible with its intrinsic lattice structure and large surface to volume ratio, it is reasonable that short lifetimes are observed in our system. A latest work on perovskite nanowire laser based on solution method has been published and it exhibits a low threshold and high quality factor;<sup>40</sup> however, our work provides a new and versatile method for synthesizing lead halide perovskite nanowire with good crystal quality, which provides us the insightful optical investigations of the perovskite nanowires.

In conclusion, organic-based lead halide perovskite nanowires with single crystalline structure were prepared successfully by a vapor phase synthesis. Using the perovskite nanowires, we have realized room-temperature visible and near-infrared solid-state nanowire lasers. Their naturally formed high-quality Fabry–Pérot mode cavities and long diffusion lengths provide adequate gain and efficient optical feedback for low-threshold optically pumped lasing. Our research will create a new platform for exploiting nanoscale optical, electronic, and optoelectronic devices on the basis of free-standing organic–inorganic perovskite nanowire with high crystal quality.

**Methods. Synthesis of  $\text{PbI}_2/\text{PbBr}_2$  Nanowire.**  $\text{PbI}_2$  powder was used as a single source put into a quartz tube in a single-zone furnace (Lindberg/Blue MTF55035C-1). The silicon substrate with oxide thickness of 285 nm (1 cm  $\times$  1 cm) was precleaned with acetone, ethanol, and water and placed in the downstream region inside the quartz tube. The quartz tube was first evacuated to a base pressure of 40 mTorr, followed by a 30

sccm flow of high purity  $\text{H}_2/\text{Ar}$  (5 vol %/95 vol %). After flowing of the gas for 30 min to eliminate the residual air, the experiment could start. The temperature and pressure inside the quartz tube were set and stabilized to 380 °C and 200 Torr. The synthesis was operated for 15 min and the furnace was allowed to cool down naturally to ambient temperature. For synthesis of  $\text{PbBr}_2$ , mica substrate (1 cm  $\times$  3 cm) was placed in the downstream region inside the quartz tube. The temperature and pressure inside the quartz tube were set and stabilized to 350 °C and 50 Torr.

**Conversion of Lead Halides to Perovskites.** The conversions were carried out using the same CVD system. Methylammonium halides  $\text{CH}_3\text{NH}_3\text{X}$  (X = I, Br, or Cl) synthesized by a solution method (detailed synthesis method can be found elsewhere)<sup>24</sup> were used as a source and placed in the center of the quartz tube while silicon wafer hosting lead halide nanowires was placed around 5 cm away from the center in the downstream region. The quartz tube was first evacuated to a base pressure of 40 mTorr, followed by a 30 sccm flow of high purity  $\text{N}_2$  gas. The temperature and pressure was stabilized at 120 °C and 50 Torr for 1 h for  $\text{CH}_3\text{NH}_3\text{I}$  and  $\text{CH}_3\text{NH}_3\text{Br}$ , and the temperature was kept at 100 °C for  $\text{CH}_3\text{NH}_3\text{Cl}$ .

**Characterizations.** The structure of the as-grown samples were characterized using an optical microscope (Olympus BX51), AFM (Veeco Dimension V) in the tapping mode, field-emission scanning electron microscopy (FE-SEM, JEOL JSM-7001F), and transmission electron microscopy with energy-dispersive X-ray spectroscopy (TEM; JEM 2100F, 200 kV and ZEISS, 120 kV). Temperature-dependent PL spectra were measured through a micro-Raman spectrometer (Horiba-JY T64000) with a single-grating setup. A series of laser lines at 325 and 473 nm (solid state laser) were used as the excitation sources. The backscattered signal was collected through a 20 $\times$  (UV) and 100 $\times$  (vis) objective and recorded by a liquid nitrogen cooled charge coupled device detector.

**Lasing Measurement and Time-Resolved Photoluminescence Spectroscopy.** The excitation pulse (400 nm) was generated by frequency doubling the 800 nm output (with a BBO crystal) from the Coherent Libra regenerative amplifier (50 fs, 1 kHz, 800 nm) that is seeded by a Coherent Vitesse oscillator (50 fs, 80 MHz). The pump laser source is introduced into a microscope (Nikon LV100) and focused onto samples via a 20 $\times$  objective (Nikon, numerical aperture: 0.4). To obtain sufficient energy injection, the laser spot is focused to  $\sim 40\ \mu\text{m}$  in diameter. The backscattered emission is collected by the same objective. The emission signal was then analyzed by a spectrometer Princeton Instrument SP2300i) equipped with a TE-cooled charge coupled device detector. For time-resolved photoluminescence spectra of single nanowire, a Coherent Mira 900 (120 fs, 76 MHz) was used as the pump laser source. The output 800 nm wavelength pulse was double frequency by a BBO crystal to 400 nm and the PL emission was collected in a standard backscattering geometry and dispersed by a 0.25 m DK240 spectrometer with 150 g/mm grating. The emission was time-resolved using an Optronic Streak Camera system that has an ultimate temporal resolution of  $\sim 10$  ps.

## ■ ASSOCIATED CONTENT

### ■ Supporting Information

Additional SEM, TEM, EDX analysis, and lasing spectra can be found in the Supporting Information. The Supporting Information is available free of charge on the ACS Publications website at DOI: 10.1021/acs.nanolett.5b01166.

## ■ AUTHOR INFORMATION

### Corresponding Author

\*E-mail address: Qihua@ntu.edu.sg.

### Author Contributions

J.X. and Q.X. conceived the idea and designed the experiment. J.X. prepared the samples and performed the SEM measurements. Q.Z. performed photoluminescence spectroscopy measurements. X.F.L. and T.C.S. conducted the lasing and time-resolved photoluminescence measurement. Y.W.Y. performed TEM measurements. C.S. performed AFM measurements. All the authors cowrote the manuscript. J.X. and X.F.L. contributed equally to this work.

### Notes

The authors declare no competing financial interest.

## ■ ACKNOWLEDGMENTS

Q.X. gratefully thanks the strong support from Singapore National Research Foundation through an Investigatorship Grant (NRF-NRFI2015-03) and a Competitive Research Program (NRF-CRP-6-2010-2). In addition, financial support from the Ministry of Education AcRF Tier 2 grants MOE2011-T2-2-051, MOE2013-T2-1-081 and MOE2014-T2-1-044, NTU Start-up grant M4080514 and SPMS collaborative Research Award M4080536 is gratefully acknowledged. This work is supported in part by the A\*Star Science and Engineering Research Council Public Sector Funding (122-PSF-0011). Q.X. and T.C.S. also acknowledge the funding of this research programme/project by the National Research Foundation (NRF), Prime Minister's Office, Singapore under its Campus for Research Excellence and Technological Enterprise (CREATE) programme.

## ■ REFERENCES

- (1) Stoumpos, C. C.; Malliakas, C. D.; Kanatzidis, M. G. *Inorg. Chem.* **2013**, *52* (15), 9019–9038.
- (2) Mitzi, D. B. *J. Mater. Chem.* **2004**, *14* (15), 2355–2365.
- (3) Cheng, Z.; Lin, J. *CrystEngComm* **2010**, *12* (10), 2646–2662.
- (4) Stranks, S. D.; Eperon, G. E.; Grancini, G.; Menelaou, C.; Alcocer, M. J. P.; Leijtens, T.; Herz, L. M.; Petrozza, A.; Snaith, H. J. *Science* **2013**, *342* (6156), 341–344.
- (5) Baikie, T.; Fang, Y.; Kadro, J. M.; Schreyer, M.; Wei, F.; Mhaisalkar, S. G.; Graetzel, M.; White, T. J. *J. Mater. Chem. A* **2013**, *1* (18), 5628–5641.
- (6) Ahmad, S.; Prakash, G. V. *J. Nanophotonics* **2014**, *8* (1), 083892.
- (7) Dong, Q.; Fang, Y.; Shao, Y.; Mulligan, P.; Qiu, J.; Cao, L.; Huang, J. *Science* **2015**, *347* (6225), 967–970.
- (8) Lee, M. M.; Teuscher, J.; Miyasaka, T.; Murakami, T. N.; Snaith, H. J. *Science* **2012**, *338* (6107), 643–647.
- (9) Liu, M.; Johnston, M. B.; Snaith, H. J. *Nature* **2013**, *501* (7467), 395–398.
- (10) Kojima, A.; Teshima, K.; Shirai, Y.; Miyasaka, T. *J. Am. Chem. Soc.* **2009**, *131* (17), 6050–6051.
- (11) Zhou, H.; Chen, Q.; Li, G.; Luo, S.; Song, T.-b.; Duan, H.-S.; Hong, Z.; You, J.; Liu, Y.; Yang, Y. *Science* **2014**, *345* (6196), 542–546.
- (12) Burschka, J.; Pellet, N.; Moon, S.-J.; Humphry-Baker, R.; Gao, P.; Nazeeruddin, M. K.; Gratzel, M. *Nature* **2013**, *499* (7458), 316–319.
- (13) National Renewable Energy Laboratory. *Best Research-Cell Efficiencies*; [http://www.nrel.gov/ncpv/images/efficiency\\_chart.jpg](http://www.nrel.gov/ncpv/images/efficiency_chart.jpg) (accessed March 20, 2015).
- (14) Xing, G.; Mathews, N.; Lim, S. S.; Yantara, N.; Liu, X.; Sabba, D.; Grätzel, M.; Mhaisalkar, S.; Sum, T. C. *Nat. Mater.* **2014**, *13* (5), 476–480.
- (15) Zhang, Q.; Ha, S. T.; Liu, X.; Sum, T. C.; Xiong, Q. *Nano Lett.* **2014**, *14* (10), 5995–6001.



- (16) Tan, Z.-K.; Moghaddam, R. S.; Lai, M. L.; Docampo, P.; Higler, R.; Deschler, F.; Price, M.; Sadhanala, A.; Pazos, L. M.; Credgington, D.; Hanusch, F.; Bein, T.; Snaith, H. J.; Friend, R. H. *Nat. Nanotechnol.* **2014**, *9* (9), 687–692.
- (17) Kagan, C. R.; Mitzi, D. B.; Dimitrakopoulos, C. D. *Science* **1999**, *286* (5441), 945–947.
- (18) Lee, Y.; Kwon, J.; Hwang, E.; Ra, C.-H.; Yoo, W. J.; Ahn, J.-H.; Park, J. H.; Cho, J. H. *Adv. Mater.* **2014**, *27* (1), 41–46.
- (19) Era, M.; Morimoto, S.; Tsutsui, T.; Saito, S. *Appl. Phys. Lett.* **1994**, *65* (6), 676–678.
- (20) Horváth, E.; Spina, M.; Szekrényes, Z.; Kamarás, K.; Gaal, R.; Gachet, D.; Forró, L. *Nano Lett.* **2014**, *14* (12), 6761–6766.
- (21) Mitzi, D. B.; Dimitrakopoulos, C. D.; Kosbar, L. L. *Chem. Mater.* **2001**, *13* (10), 3728–3740.
- (22) Liu, X.; Ha, S. T.; Zhang, Q.; de la Mata, M.; Magen, C.; Arbiol, J.; Sum, T. C.; Xiong, Q. *ACS Nano* **2015**, *9* (1), 687–695.
- (23) Im, J.-H.; Luo, J.; Franckevičius, M.; Pellet, N.; Gao, P.; Moehl, T.; Zakeeruddin, S. M.; Nazeeruddin, M. K.; Grätzel, M.; Park, N.-G. *Nano Lett.* **2015**, *15* (3), 2120–2126.
- (24) Ha, S. T.; Liu, X.; Zhang, Q.; Giovanni, D.; Sum, T. C.; Xiong, Q. *Adv. Opt. Mater.* **2014**, *2* (9), 838–844.
- (25) Wang, Y.; Gould, T.; Dobson, J. F.; Zhang, H.; Yang, H.; Yao, X.; Zhao, H. *Phys. Chem. Chem. Phys.* **2014**, *16* (4), 1424–1429.
- (26) D’Innocenzo, V.; Grancini, G.; Alcocer, M. J. P.; Kandada, A. R. S.; Stranks, S. D.; Lee, M. M.; Lanzani, G.; Snaith, H. J.; Petrozza, A. *Nat. Commun.* **2014**, *5*, 3586.
- (27) Ashcroft, N. W.; Mermin, N. D. *Solid State Physics*; Holt Rinehart & Winston: New York, 1976.
- (28) Poglitsch, A.; Weber, D. J. *Chem. Phys.* **1987**, *87* (11), 6373.
- (29) Schenk, H. P. D.; Leroux, M.; de Mierry, P. J. *Appl. Phys.* **2000**, *88* (3), 1525–1534.
- (30) Yang, W. F.; Xie, Y. N.; Pan, Z. Y.; Hong, M. H.; Wu, Z. Y.; Wong, L. M.; Wang, S. J.; Wang, C. F.; Lee, A. Y. S.; Gong, H. *EPL* **2012**, *99* (2), 27003.
- (31) Huang, M. H.; Mao, S.; Feick, H.; Yan, H.; Wu, Y.; Kind, H.; Weber, E.; Russo, R.; Yang, P. *Science* **2001**, *292* (5523), 1897–1899.
- (32) Oulton, R. F.; Sorger, V. J.; Zentgraf, T.; Ma, R.-M.; Gladden, C.; Dai, L.; Bartal, G.; Zhang, X. *Nature* **2009**, *461* (7264), 629–632.
- (33) Zhang, Q.; Li, G.; Liu, X.; Qian, F.; Li, Y.; Sum, T. C.; Lieber, C. M.; Xiong, Q. *Nat. Commun.* **2014**, *5*, 4953.
- (34) Zhang, C.; Zou, C.-L.; Yan, Y.; Hao, R.; Sun, F.-W.; Han, Z.-F.; Zhao, Y. S.; Yao, J. J. *Am. Chem. Soc.* **2011**, *133* (19), 7276–7279.
- (35) Guo, P.; Zhuang, X.; Xu, J.; Zhang, Q.; Hu, W.; Zhu, X.; Wang, X.; Wan, Q.; He, P.; Zhou, H.; Pan, A. *Nano Lett.* **2013**, *13* (3), 1251–1256.
- (36) Pan, A.; Zhou, W.; Leong, E. S. P.; Liu, R.; Chin, A. H.; Zou, B.; Ning, C. Z. *Nano Lett.* **2009**, *9* (2), 784–788.
- (37) Piccione, B.; Cho, C.-H.; van Vugt, L. K.; Agarwal, R. *Nat. Nanotechnol.* **2012**, *7* (10), 640–645.
- (38) Saxena, D.; Mokkapati, S.; Jagadish, C. *IEEE Photonics J.* **2012**, *4* (2), 582–585.
- (39) Leijtens, T.; Stranks, S. D.; Eperon, G. E.; Lindblad, R.; Johansson, E. M. J.; McPherson, I. J.; Rensmo, H.; Ball, J. M.; Lee, M. M.; Snaith, H. J. *ACS Nano* **2014**, *8* (7), 7147–7155.
- (40) Zhu, H.; Fu, Y.; Meng, F.; Wu, X.; Gong, Z.; Ding, Q.; Gustafsson, M. V.; Trinh, M. T.; Jin, S.; Zhu, X. Y. *Nat. Mater.* **2015**, *14* (6), 636–642.